

Experimental Analysis of Air Pads with Micro Holes

*Original*

Experimental Analysis of Air Pads with Micro Holes / Belforte, Guido; Colombo, Federico; Raparelli, Terenziano; Trivella, Andrea; Viktorov, Vladimir. - In: TRIBOLOGY TRANSACTIONS. - ISSN 1040-2004. - STAMPA. - 56:2(2013), pp. 169-177. [10.1080/10402004.2012.734547]

*Availability:*

This version is available at: 11583/2504422 since: 2020-07-02T18:43:54Z

*Publisher:*

Taylor and Francis

*Published*

DOI:10.1080/10402004.2012.734547

*Terms of use:*

This article is made available under terms and conditions as specified in the corresponding bibliographic description in the repository

*Publisher copyright*

(Article begins on next page)

# EXPERIMENTAL ANALYSIS OF AIR PADS WITH MICRO-HOLES

**G. Belforte, F. Colombo, T. Raparelli, A. Trivella, V. Viktorov**

Department of Mechanical and Aerospace Engineering, Politecnico di Torino, Italy  
[guido.belforte@polito.it](mailto:guido.belforte@polito.it), [federico.colombo@polito.it](mailto:federico.colombo@polito.it), [terenziano.raparelli@polito.it](mailto:terenziano.raparelli@polito.it),  
[andrea.trivella@polito.it](mailto:andrea.trivella@polito.it), [vladimir.viktorov@polito.it](mailto:vladimir.viktorov@polito.it)

**Keywords:** *Air bearings - inherent orifices - micro hole feeding system - stiffness optimization*

## INTRODUCTION

Air pads are widely used in linear guides and precision systems with high positioning accuracy (machine tools and measuring machines). The feeding systems generally feature calibrated holes and can be provided with supply grooves. The types most commonly described in the literature are inherent orifice supply systems, where the supply hole is produced with a twist drill and normally has a diameter ranging from 0.15-0.4 mm. For example, [1-5] investigate load capacity, stiffness and air consumption, while [6] compares this type of bearing and porous bearings. Porous pads have higher load capacity than inherent orifices, but permeability must be lower to achieve good stiffness and low air consumption. In addition, the machining processes required to obtain suitable levels of permeability are not economical. In [7-9], air hammer instability, damping and tilting effect are investigated for different geometric parameters. Numerical methods are generally used to predict the pressure distribution in fluid film bearings, considering the discharge coefficient as a constant number [10] or as a function of the Reynolds number, supply hole geometry and fluid film thickness [11,12]. More recently [13], pressure distribution has been determined using a three dimensional CFD code, while the effect of the number of pressurized pad supply holes was investigated experimentally in [14].

Theoretical studies show that the performance of pressurized gas bearings with inherent orifices can be improved by using an adequate number of micro-holes with diameter under 0.1 mm. Though

several studies have been conducted in recent years to analyze the behavior of different types of gas bearings, especially for high speed rotations [15-18], only a few works can be found in the literature for micro-hole pressurized gas bearings because of the difficulty involved in producing the orifices. In [19], the pressure distribution under pads with 30  $\mu\text{m}$  diameter micro-holes fabricated using MEMS technology is measured. A numerical study of the performance of micro-drilled thrust bearings considering the discharge coefficient of the micro-holes is discussed in [20], where it is noted that laser technology has recently made it possible to produce micro-holes on metallic substrates with good repeatability and precision at reasonable cost, thus simplifying the manufacturing process.

This paper presents an experimental study of air pads with micro-holes fabricated using laser technology. Circular and rectangular pads are considered, with supply hole diameters in the 0.05-0.1 mm range. The pads under test, the test bench and the experimental procedure are described. The influence of the number of supply holes and of their diameter and position on results is evaluated.

## PADS UNDER TEST

Circular and rectangular anodized aluminum pads, designated as types “C” and “R” respectively, were tested. Dimensions were identical for each shape. Pad geometry is illustrated in Figure 1, while Table 1 shows the number  $N$  of supply holes, their nominal diameter  $d_n$  and their mean diameter  $d_m$  measured with a microscope ( $d_m = \frac{1}{N} \sum_{i=1}^N d_{mi}$ ,  $d_{mi} = \frac{d'_{mi} + d''_{mi}}{2}$ ,  $d'_{mi}$ ,  $d''_{mi}$  are two perpendicular hole diameters). The table also shows measured average roughness  $R_a$  (the mean of roughness values measured on different areas of the pad;  $R_{a,min} = 0.16 \mu\text{m}$ ,  $R_{a,max} = 0.20 \mu\text{m}$ ).

Values for  $N$  and  $d_h$  were chosen in order to compare pads having the same total supply hole surface area (pads 1 and 3; 8 and 9).

Circular pads have a diameter  $D = 50$  mm and a height of 14 mm. Supply holes are equispaced around a circumference of diameter  $D_h$  equal to 31 mm for pads 1, 2, 3 and to 39 mm for pad 4. Rectangular pads have dimensions  $L_1 \times L_2 = 60 \times 30$  mm and height is 13 mm; supply holes are located on an internal rectangle of dimensions  $l_1 \times l_2 = 43 \times 19$  mm. For pads 5 and 6, the holes are located midway along the length of each side, while for pads 7, 8 and 9, the holes are equispaced on each side. In figure 2 one circular and one rectangular pad are shown.

Both pad types feature (Figure 3) internal supply lines  $I$  with diameter 1 mm, connected by slots 2 which are 6.5 mm wide and 2 mm deep. Micro-holes 0.4 mm in length are drilled in the lower part of lines  $I$ . A plate element screwed onto the pad seals grooves 2 by means of O-rings. Load system housing 3 is located at the center of the pad. The housing is provided with a ball joint to ensure that the pad is correctly positioned under load.

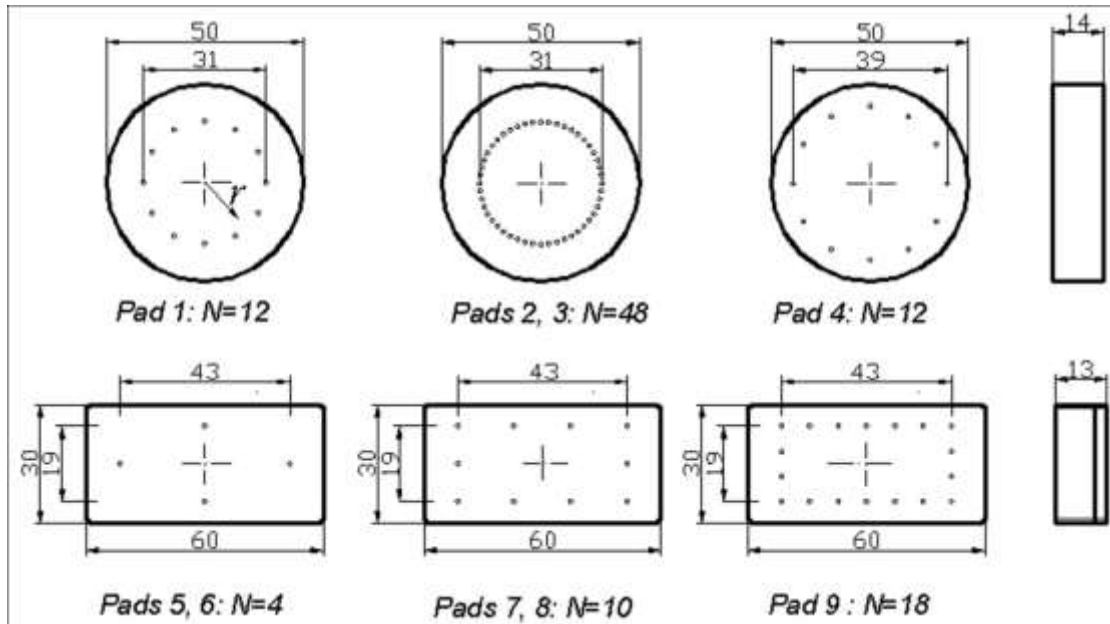


Figure 1. Schematic views of tested pads

The schematic view in Figure 4 shows the radial section of one circular pad, indicating the layout of the internal lines, the micro-holes and the air supply port in the clamping plate. A non-supplied micro-hole of diameter  $d_n$  (probe hole) enables pressure readings to be taken at a predetermined point of the air gap. The photo in Figure 5 shows the back side of the pad.

Loading, clamping and sealing systems for the rectangular pads are similar to those for the circular pads, though in this case the rectangular clamping plate is the same size as the pad.

Figure 6 is an enlarged view under the microscope of several supply holes of different pads, showing that there is good repeatability and sufficient precision. With the exception of the first three pads, the difference between the nominal diameter  $d_n$  and the measured mean diameter  $d_m$  is about 5%.

## **TEST RIG DESCRIPTION AND EXPERIMENTAL SET-UP**

Static characteristics of the pads were determined experimentally with the test bench shown in Figures 7 and 8. The bench consists essentially of a rigid structure *1* and a stationary member *2* carrying pad *3*, which is loaded by means of screw and handwheel *4*. Pressure under the pad is measured with a piezoresistive sensor PT with  $10^{-4}$  MPa resolution, connected to a 0.2 mm diameter measuring hole drilled in the stationary member. The latter can be moved radially

Pad No.	Pad type	$N$	$D_h$ (mm)	$d_n$ (mm)	$d_m$ (mm)	$Ra$ ( $\mu\text{m}$ )
1	C	12	31	0.100	0.111	0.16
2	C	48	31	0.100	0.116	0.19
3	C	48	31	0.050	0.061	0.18
4	C	12	39	0.100	0.104	0.16
5	R	4	-	0.070	0.074	0.16
6	R	4	-	0.100	0.100	0.15
7	R	10	-	0.054	0.053	0.18
8	R	10	-	0.070	0.072	0.20
9	R	18	-	0.054	0.053	0.17

Table 1. *Geometric parameters of pads*

or rotated in order to measure the pressure at each point of the air gap. Radial and angular positions of the measuring hole with respect to the center of the pad are given by a potentiometric displacement transducer and a goniometer. Air gap height is measured by means of two micrometric inductive probes 5 with 0.1  $\mu\text{m}$  resolution, located at the center and the edge of the pad. Force is measured by load cell 6 with 2kN full scale and 0.2 N resolution, while supply pressure is regulated by means of pressure regulator 7 and measured by manometer 8 with 5 kPa resolution. Air flow rate is measured by two rotameters 9 with ranges of 0.03-0.7 l/min A.N.R. and 0.3-8 l/min A.N.R., accuracy class 1.6, situated upstream of the pad. A thermocouple measures supply air temperature. High efficiency air filters 10 (97% and 99% efficiency with 0.1  $\mu\text{m}$  diameter particles) are used to prevent supply hole clogging problems.

Load consumption and air consumption values are heavily influenced by the height  $h$  of the air gap between the pad and the stationary bearing member. The measurement procedure shown



Figure 2. Photo of a circular and a rectangular pad

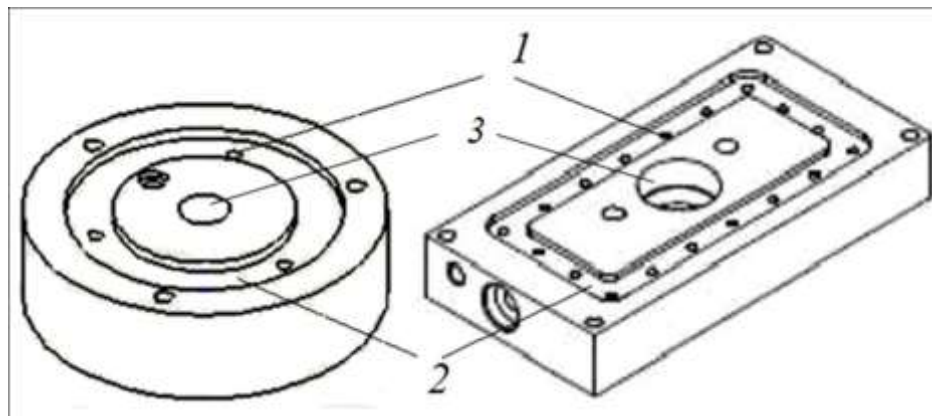


Figure 3. Layout of internal supply lines and holes.

in the flowchart in Figure 9 was developed to ensure correct air gap height readings and good repeatability of results. In this procedure, the pad is initially supplied at operating pressure and pushed against the stationary member by means of the handwheel with a force sufficient to guarantee contact and bring the flow rate measured by the more sensitive rotameter to zero. The inductive probes are then zeroed and the handwheel is turned to set the air gap at the desired height. Load capacity and air flow are measured at increasing air gap heights, where the latter are obtained

as the average of the readings of the two probes. To take the inevitable micro distortions under load into account, checks were carried out to ensure that the probe  $h$  readings were repeatable during measurements. For certain air gap height settings, the air supply to the pad is turned off and then back on: if  $h$  is found to be repeatable, the reading corresponds to the actual air gap height, and force and air flow are measured. If not, the air gap is adjusted by means of the handwheel until the desired repeatability is achieved when air supply is turned off and on again. The flowchart of Figure 9 shows the procedure details. For each air gap height setting, the pad supply pressure is checked and if necessary corrected. Several load and flow rate curves were determined for each pad, and the curve showing the best repeatability was selected. With this procedure, the repeatability error for  $h$  measurements was kept within approximately  $\pm 1 \mu\text{m}$ .

## EXPERIMENTAL RESULTS

Results for load capacity  $F$ , stiffness  $K$  and mass air flow  $G$  as a function of air gap  $h$  will be discussed in this paragraph, where several pressure distributions will also be presented for circular pads. All measurements were performed with a supply pressure  $p_s$  of 0.4 MPa

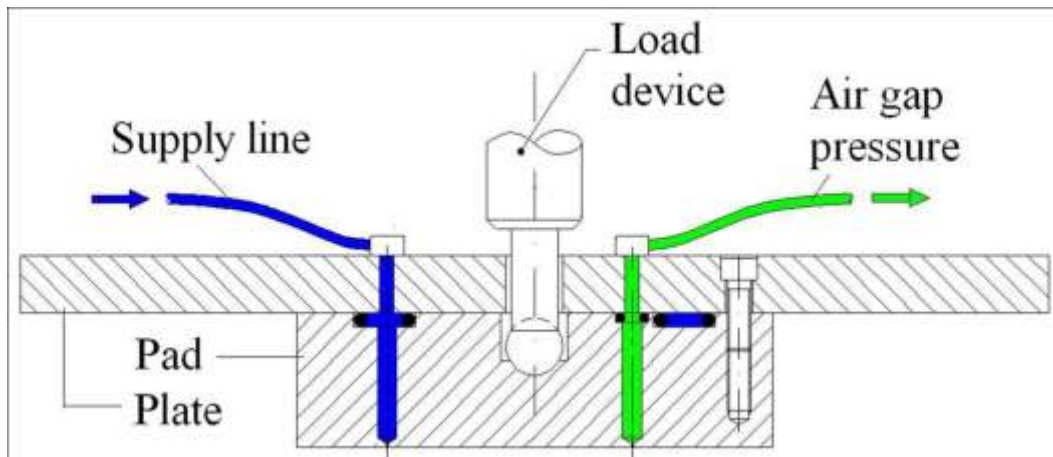


Figure 4: Internal lines of a circular pad



at a temperature of about 24 °C. Stiffness is calculated as  $K=-dF/dh$  , by differentiating the measured load capacity and then fitting with interpolating parabolic curves. Data are shown for air gap heights over 5µm in order to take the pad's geometric flatness tolerances (approximately 1 µm), distortions under load (about 1 µm) and the measurement error for  $h$  into account. In addition, these pads normally operate with air gaps in excess of 5 µm.

### **Circular pads**

Figures 10-12 show the results for load capacity, stiffness and air consumption for circular pads. Load capacity is maximum at small air gap heights. The highest load capacity and air consumption are achieved with the largest number of holes and the largest supply hole diameters (pad 2).

For pads with the same hole diameters and supply hole positions (pads 1 and 2), load capacity and consumption rise significantly as  $N$  increases from 12 to 48. As regards stiffness, pad 1 is to be preferred, as its maximum stiffness is 20% higher than that of pad 2.

With  $N$  and hole position constant (i.e., comparing pads 2, 3), load capacity increases as  $d_n$  increases from 0.05 to 0.1 mm, and this is more evident at high  $h$  (Figure 10). Conversely, when  $d_n$  decreases from 0.1 to 0.05 mm, maximum stiffness increases significantly and can be obtained at lower  $h$  (Figure 11). As can be seen from the data, the air gap at which maximum stiffness is achieved is a function of  $N$  and  $d_n$ . This gap value increases both



Figure 5: Back side of a circular pad

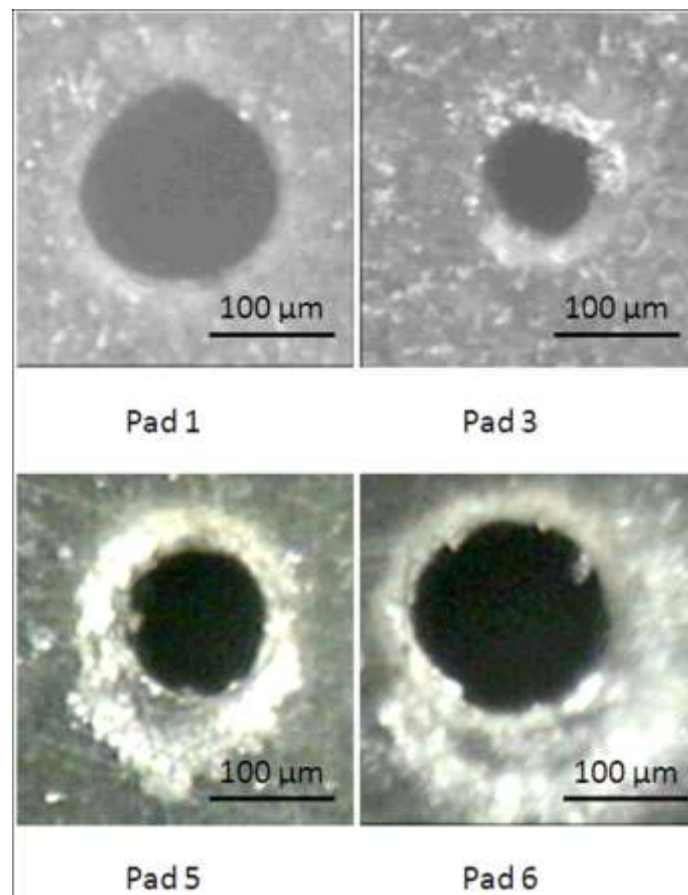


Figure 6. Enlargement of same representative holes in pads 1, 3, 5, 6.

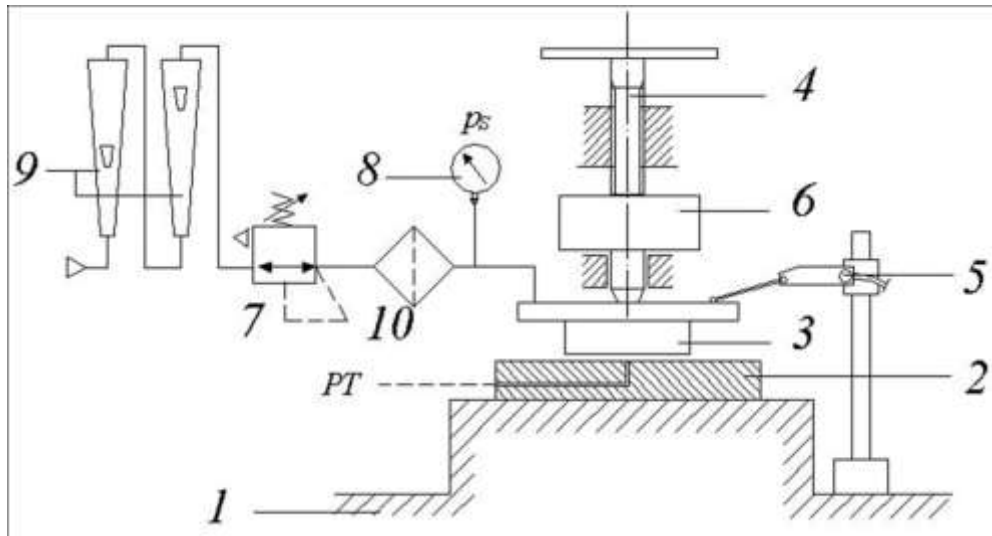


Figure 7. Schematic view of the test bench

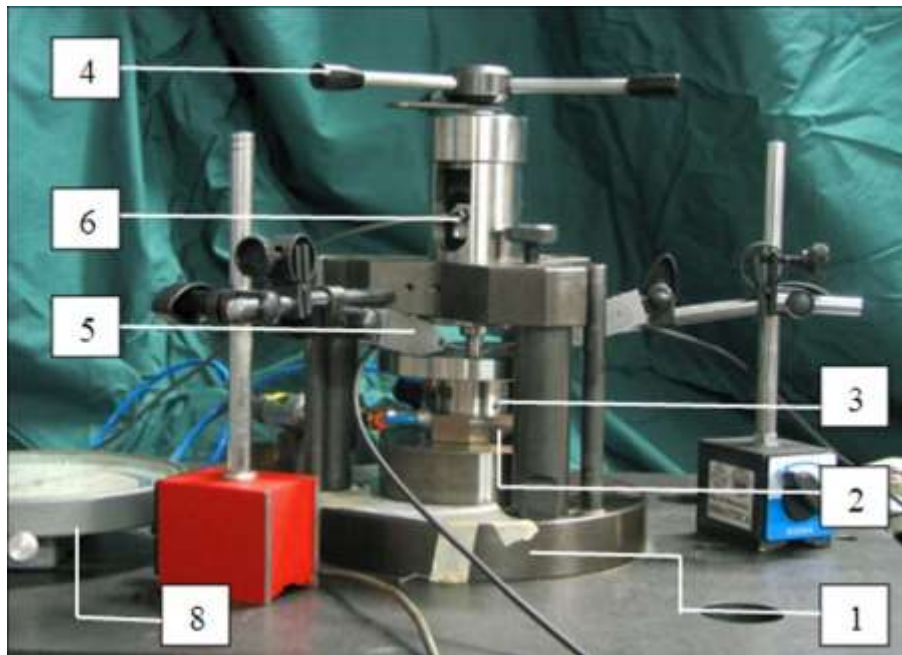


Figure 8. Photo of the test bench

when  $N$  is increased while maintaining the same  $d_n$ , and when  $d_n$  is increased while maintaining the same  $N$ .

For any given  $N$  and  $d_n$ , load capacity and stiffness change significantly with different hole positions. A comparison between pads 1 and 4 shows that the latter has a lower load capacity and higher stiffness, while the flow rate remains essentially the same. Maximum stiffness is achieved for smaller air gap heights.

In designing the pad, it is important to find the optimal number and diameter of the supply holes to obtain the required load capacity and maximize stiffness at a given air gap. It is clear from an analysis of experimental results that load capacity improves when  $N$  alone is increased and when  $d_n$

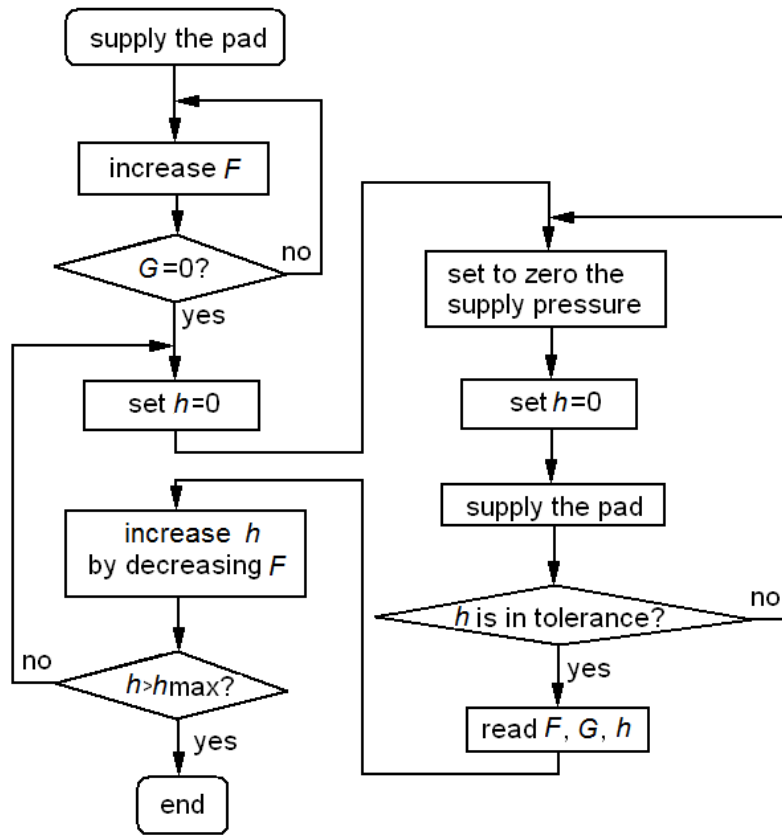


Figure 9. Flowchart of the experimental procedure

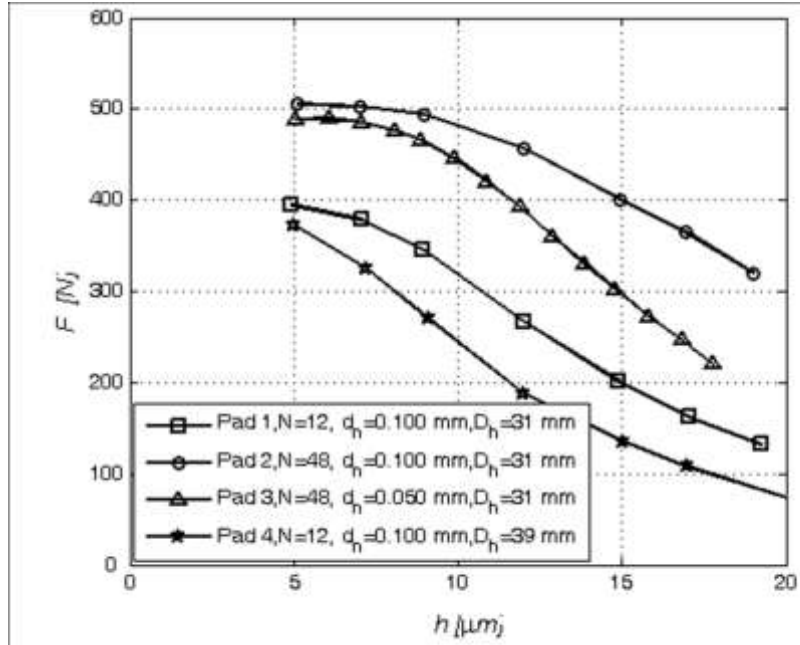


Figure 10. Load capacity  $F$  vs.  $h$ , pads 1-4.

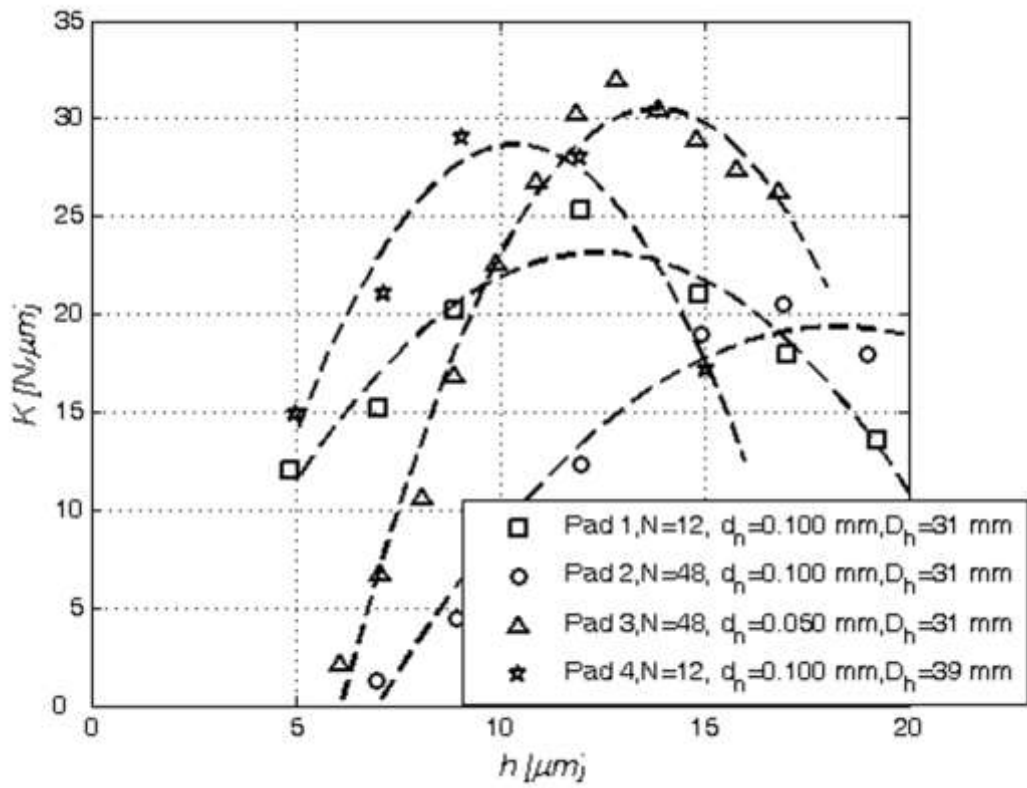


Figure 11. Stiffness  $K$  vs.  $h$ , pads 1-4.

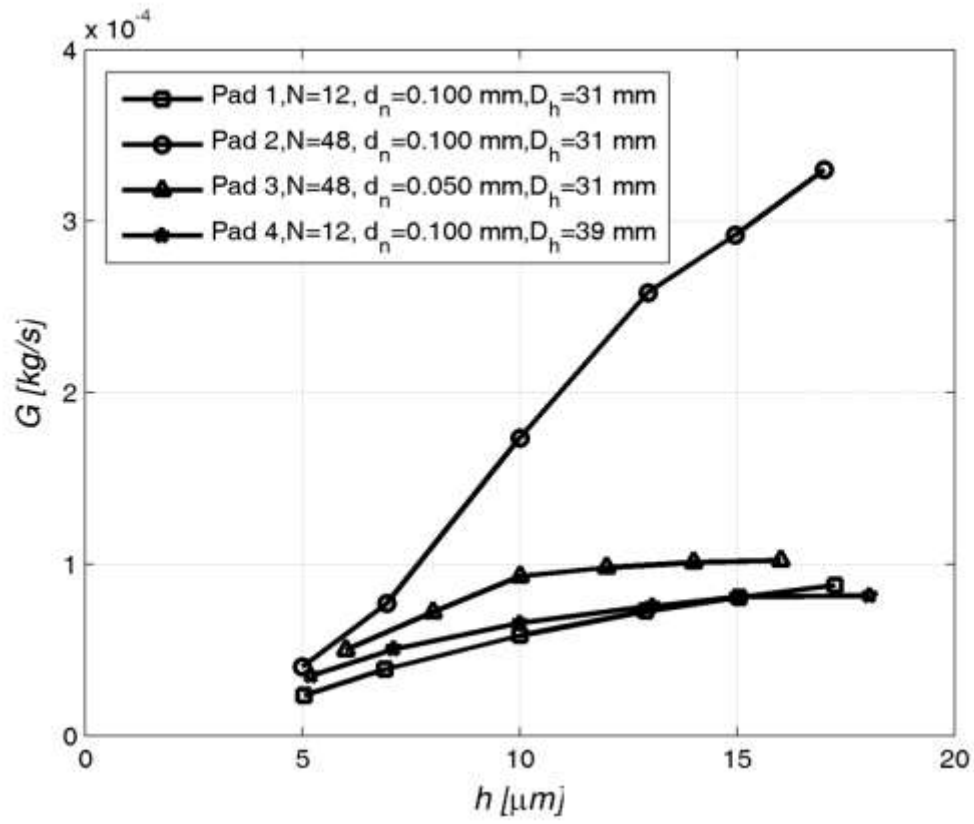


Figure 12. Mass flow rate  $G$  vs.  $h$ , pads 1-4.

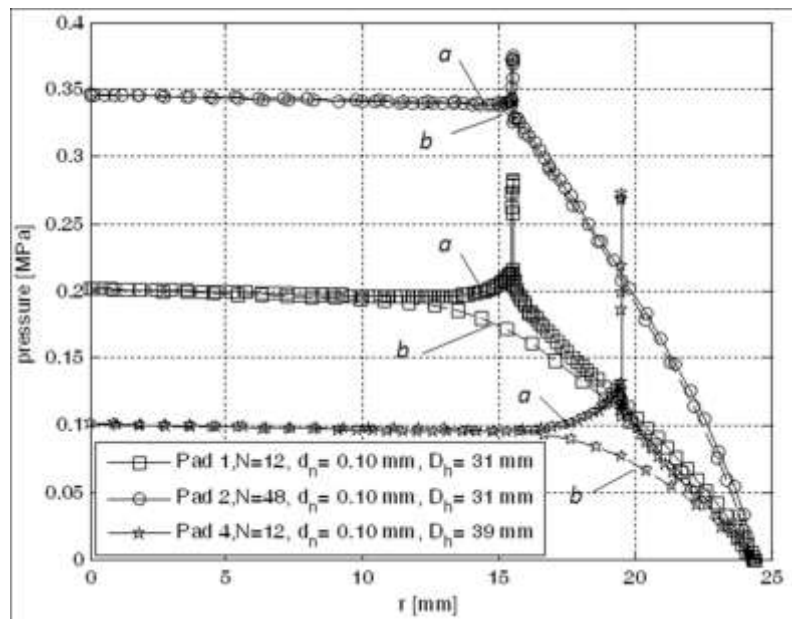


Figure 13. Radial pressure distribution for pads 1, 2, 4.

alone is increased, but maximum stiffness moves towards higher air gaps. Pad performance can be optimized by changing both the number of holes and their diameter. In particular, this maximizes stiffness at the required air gap. A criterion used is to modify  $d_n$  and  $N$  while maintaining a constant total surface area for the supply holes ( $d_n \propto 1/\sqrt{N}$ ). As can be seen by comparing the maximum stiffness position of pads 1 and 3, moreover, the effect of increasing  $N$  is balanced by the effect of decreasing  $d_n$ . This position is almost the same, and the difference is comparable to the air gap measurement error (Figure 11). These pads have a similar air consumption because the total supply hole surface area is the same, the only difference being that pad 3 reaches choked flow at the supply holes with smaller air gaps (Figure 12). Sonic flow conditions through the supply holes improve pad performance, as in this case the operating characteristics depend only on the height of the air gap.

Examining the pressure distribution provides information which can be useful in understanding pad behavior. Figure 13 shows the radial pressure distributions obtained with pads 1, 2 and 4, measured both in a plane passing through one of the supply holes (curves *a*), and in the midplane between two adjacent holes (curves *b*). The axially symmetric pressure distribution is roughly constant over the entire area inside the array of supply holes. A comparison of curves 1 and 4 shows that varying  $D_h$  alone does not change the radial pressure gradient in the outer drilling area. Ambient pressure is reached at a chamfer on the outside diameter of the pad.

Figure 14 shows a detail of the distribution at the inlet port;  $r_l$  is the radial distance measured from the center of the hole. The peak pressure in the inlet port and the pressure depression phenomenon [8] are particularly clear. The relative maximum pressure in the inner zone is slightly higher than that in the outer zone due to the filling pressure.

Pressure distributions in the circumferential direction are shown in Figure 15, where  $c$  is the circumferential coordinate measured by choosing the center of the supply hole as the origin. As can be seen, the presence of numerous supply holes gives an

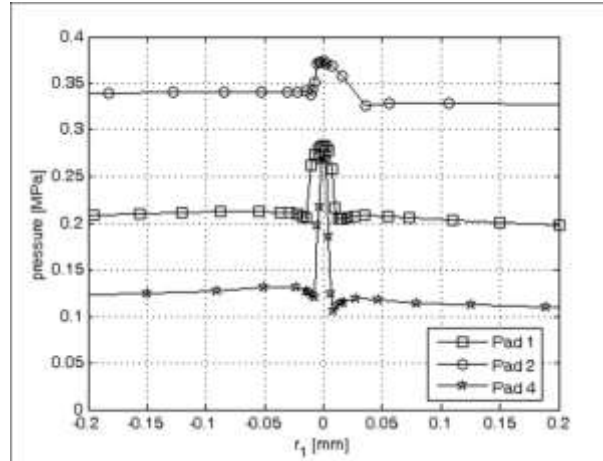


Figure 14. Detail of radial pressure distributions close to one supply hole.

almost constant pressure distribution along the circumferential direction.

Measuring the pressure distribution is particularly useful in determining supply hole discharge coefficients. For the micro-holes examined here, it should be borne in mind that the relatively large size of the measuring hole ( $200\text{ }\mu\text{m}$ ) affects the pressure measurement near the inlet hole. In this case, in fact, the hole is far less sensitive to sudden changes in pressure at the entrance of the air gap, and the measured values differ significantly from the actual values. Considering also that the smaller the holes, the more difficult it will be to center the measuring hole relative to the supply port, the method for determining the discharge coefficients from pressure readings taken near the supply holes could be less accurate in the case of pads with micro supply holes. An alternative solution proposed in [21] makes it possible to identify the discharge coefficient more readily by



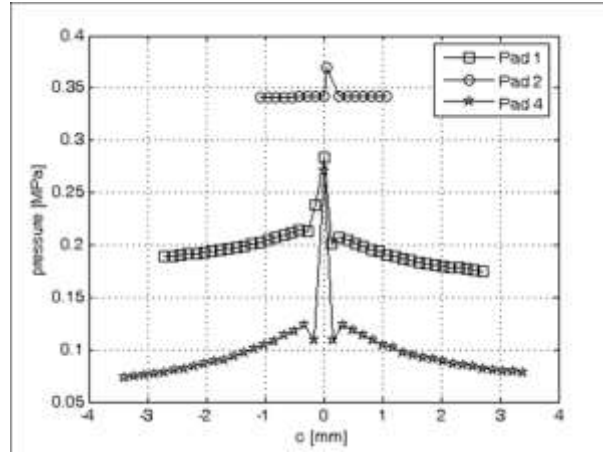


Figure 15. Circumferential pressure distributions for pads 1, 2, 4.

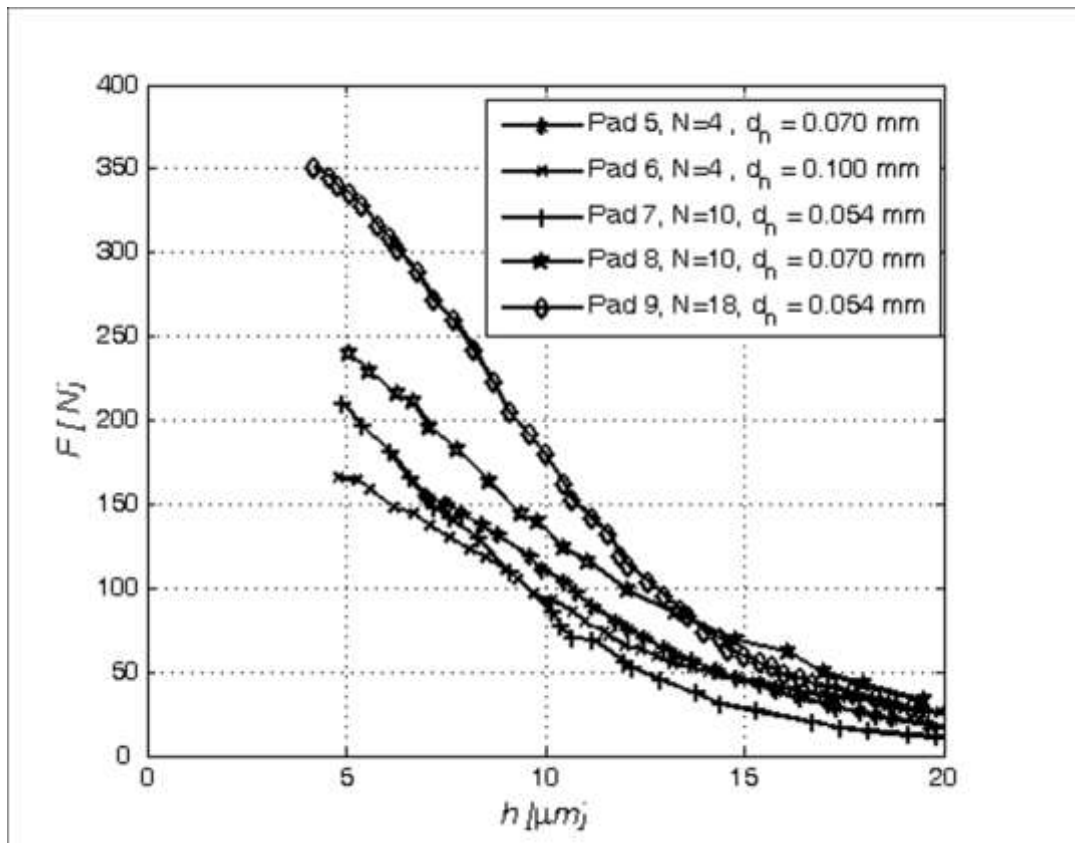


Figure 16. Load capacity  $F$  vs.  $h$ , pads 5-9.

measuring pressure at points located at a considerable distance from the supply holes.

## Rectangular pads

In general, variations in parameters  $N$  and  $d_n$  tend to produce similar effects for pads of different shapes and sizes. Figures 16-18 show the results for rectangular pads 5, 6, 7, 8 and 9. At constant  $N$  (comparison between pads 7, 8) and increasing  $d_n$ , there is still an increase in load capacity and a reduction in maximum stiffness (Figures 16, 17). Considering the same  $d_n$  (comparison between 5, 8 and 7, 9, Fig. 17), increasing  $N$  causes an increase in load capacity. However, there are some differences in stiffness behavior compared to that observed for circular pads; this is due to the different geometry and different ranges of  $d_n$  and  $N$  investigated. With constant  $d_n$ , for example, there is no reduction in  $K$  as  $N$  is increased (comparison between pads 7, 9, Figure 17). In fact, for rectangular pad 9, the distance between

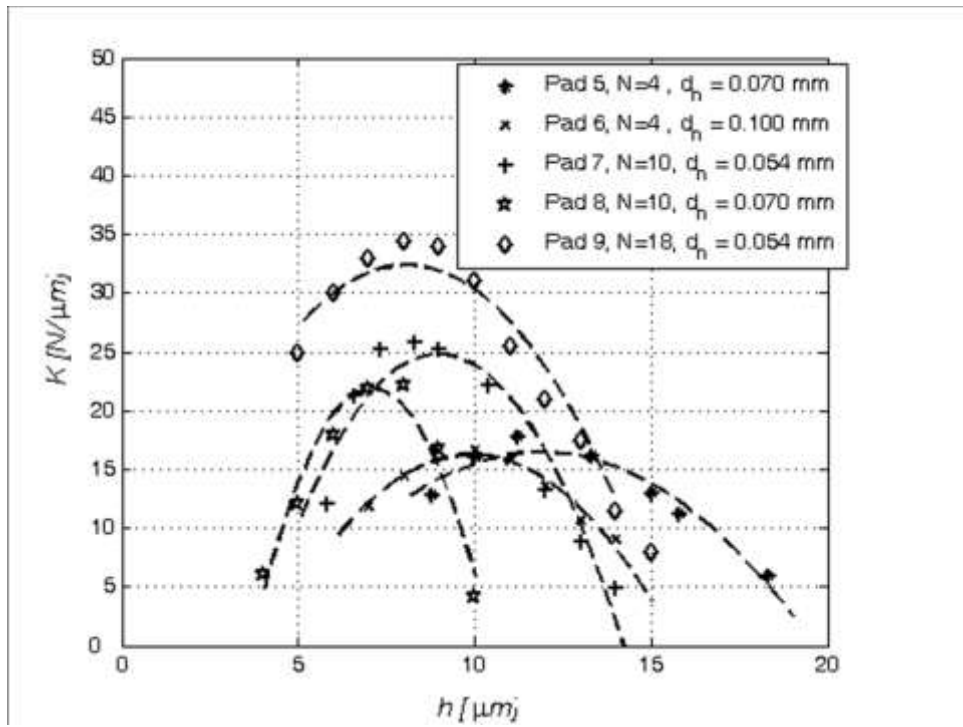


Figure 17. Stiffness  $K$  vs.  $h$ , pads 5-9.

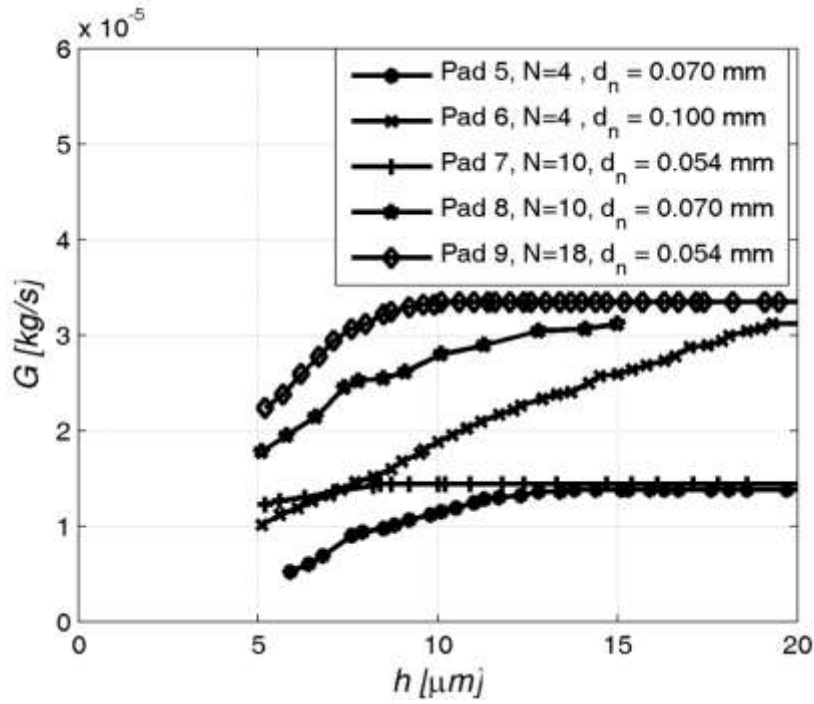


Figure 18. Mass flow rate  $G$  vs.  $h$ , pads 5-9.

two adjacent holes is more than three times greater than for circular pad 3: this entails less uniform pressure distribution in the first pad. With constant  $d_n$ , moreover (comparison between pads 5, 8 and 7, 9), maximum stiffness does not shift towards higher air gaps as  $N$  is increased, as this effect is apparent only for a significant increase in  $N$ . For the examined circular pads, the number of supply holes increases by a factor of 4, while for the rectangular pads it increases by a factor of around 2. Consequently, the distance between two maxima of stiffness is comparable to the precision in measuring  $h$ . The same considerations apply when comparing pads 7 and 8, which have the same  $N$  but quite similar values of  $d_n$ . Finally, comparison with the same total supply hole surface area (pads 8, 9) confirms the observations made for circular pads.

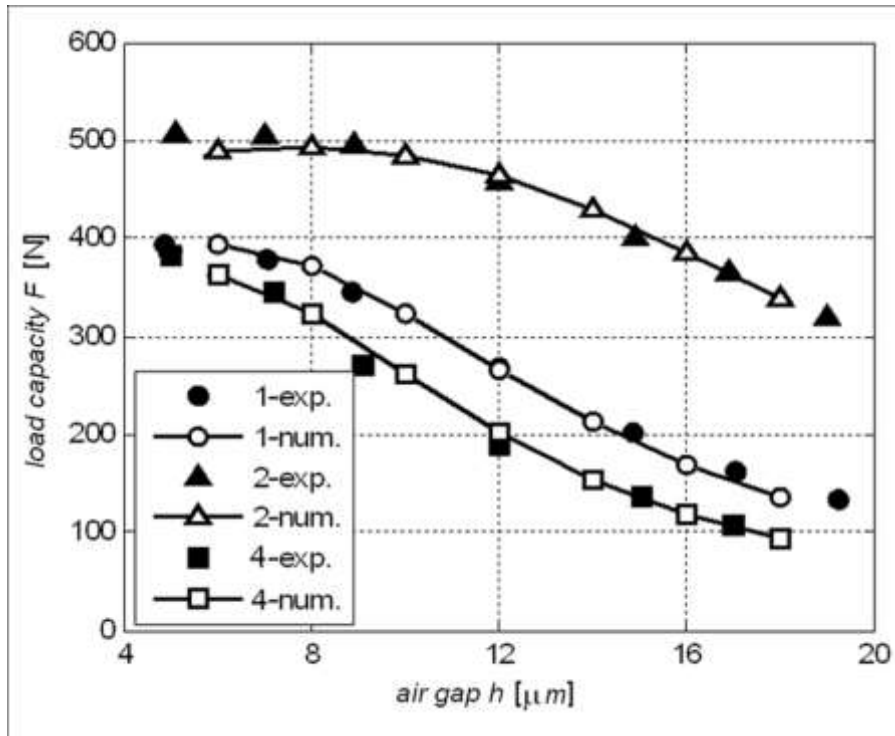


Figure 19. Experimental and numerical load capacity  $F$  vs.  $h$ , pads 1, 2, 4.

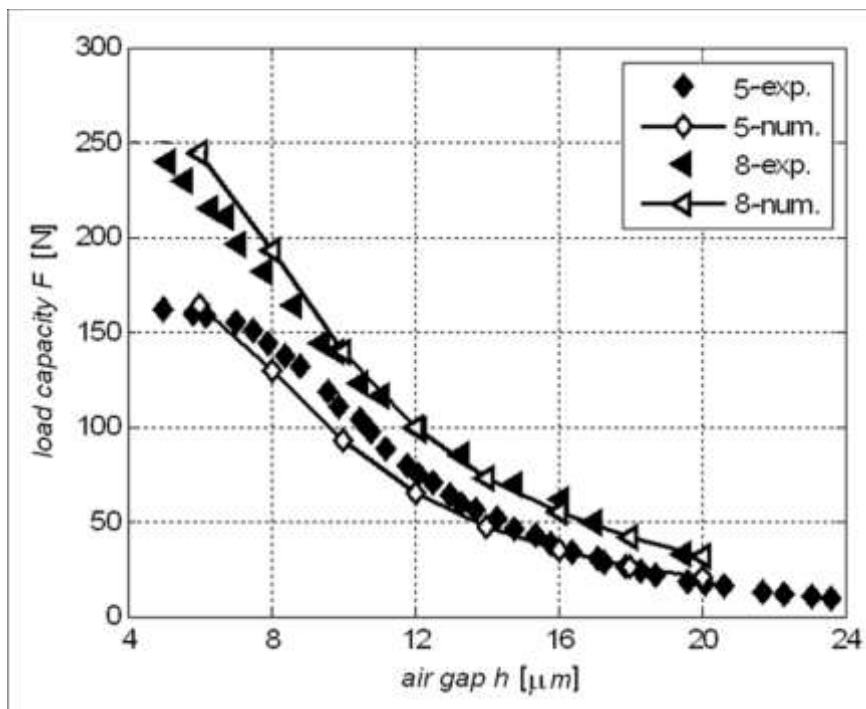


Figure 20. Experimental and numerical load capacity  $F$  vs.  $h$ , pads 5, 8.

## NUMERICAL COMPARISON

In Figures 19 and 20, several of these pads are compared with numerical results obtained with a distributed parameters model that integrates the Reynolds equations for compressible fluids. The equation was discretized with finite difference technique. The model uses the formulation for the discharge coefficients  $C_d$  validated in [11] for supply hole diameters ranging from 0.2 to 0.4 mm:

$$C_d = 0.85 (1 - e^{-8.2(h/d)})(1 - e^{-0.001 Re})$$

where  $h$ ,  $d$  and  $Re$  are respectively the air height gap, the mean diameter of the supply hole and the Reynolds number calculated considering the circular passage section of the holes. This experimental activity was also carried out to verify whether the same formulation can also be used for smaller hole diameters. With this formulation, the theoretical curves are a fairly good fit with the experimental data. It is interesting to note that this formula, which was obtained for larger holes, also works well for micro-holes.

## CONCLUSIONS

Pneumostatic pad performance can be optimized achieved using several supply holes less than 0.1 mm in diameter, fabricated using laser technology with good repeatability and precision up to dimensions close to 0.05 mm.

Optimization depends on pad geometry, and normally aims at maximizing stiffness. There is a combination of supply hole position, number and diameter that maximizes pad stiffness for a given air gap height. For any given supply hole diameter  $d_n$  and number  $N$ , load capacity can be maximized by choosing a inner supply circumference or rectangle of dimensions scaled by a factor of 0.6-0.7 with respect to the pad's external dimensions. Then, by modifying  $d_n$  and  $N$  while maintaining the total supply surface area constant, it is possible to improve stiffness at a given air

gap and to limit air consumption. Among all pads tested, the most interesting results were obtained for samples 3 and 9.

In addition, this experimental investigation demonstrated that the discharge coefficient formula presented in [11] also works well for micro-holes.

## REFERENCES

- (1) H. Mori, H. Yabe (1964), “Analysis of externally pressurized circular thrust gas-bearing with multiple supply holes”, Trib. Transactions, **7**, 3, pp. 269-276.
- (2) H. Mori, H. Yabe, K. Ohnishi (1966), “Analysis of externally pressurized rectangular pads with multiple supply holes”, Trib. Transactions, **9**, 4, pp. 391-40.
- (3) Dudgeon E. H., Lowe I. R. (1971), “An investigation of centrally-fed, circular, inherently-compensated, aerostatic thrust bearings”, Proc. “Gas Bearing Symposium”, University of Southampton, Department of Mechanical Engineering, University of Southampton, March 5, 1971.
- (4) Chen K., Rowe W. B. (1975), “A selection strategy for the design of externally pressurized journal bearings”, Tribol. Intern., **28**, pp. 465-474.
- (5) Sharma S. C., Jain S. C., Bharuka D. K. (2002), “Influence of recess shape on the performance of a capillary compensated circular thrust pad hydrostatic bearing”, Trib. Intern., **35**, pp. 347-356.
- (6) Fourka M., Bonis M. (1997), “Comparison between externally pressurized gas thrust bearings with different orifice and porous feeding systems”, Wear, **210**, pp. 311-317.
- (7) Stiffler A. K. (1974), “Analysis of the stiffness and damping of an inherently compensated, multiple-inlet, circular thrust bearing”, Journal of Lubrication Technology, pp. 329-336.

- (8) Blondeel E., Snoeys R., Devrieze L. (1980), "Dynamic Stability of Externally Pressurized Gas Bearings", *Journal of Lubrication Technology* **102**,10, pp. 511-519.
- (9) Al-Bender F., Van Brussel H. (1992), "Tilt characteristics of circular centrally fed aerostatic bearings", *Trib. Intern.* **25** (3), pp. 189-197.
- (10) S. Cioc, F. Dimofte, T. G. Keith Jr, D. P. Fleming, (2003), "Computation of pressurized gas bearings using the CE/SE method", *Trib. Transactions*, 46:1, pp.128-133.
- (11) Belforte G., Raparelli T., Viktorov V., Trivella A. (2007), "Discharge coefficients of orifice-type restrictor for aerostatic bearings", *Trib. Intern.* **40**, pp. 512-521.
- (12) Belforte G., Raparelli T., Trivella A., Viktorov V. (2011), "Identification of discharge coefficients of orifice-type restrictors for aerostatic bearings and application examples", *New Tribological Ways*, Chapter 18, INTECH, pp. 359-380.
- (13) A. Sescu, C. Sescu, F. Dimofte, S. Cioc, A. A. Afjeh, R. Handschuh, (2009), "A study of the steady-state performance of a pressurized air wave bearing at concentric position", *Trib. Transactions*, **52**: 4, pp. 544-552.
- (14) Belforte G., Colombo F., Raparelli T., Trivella A., Viktorov V. (2009), "Aerostatic thrust bearings: experimental comparison between different feeding solutions", *2<sup>nd</sup> European Conference on Tribology ECOTRIB 2009*, **1**, June 07-10, pp.407-412.
- (15) S. M. Yao, H. W. Ma, L. Q. Wang (2011), "Aerostatic and aerodynamic performance of a herringbone thrust bearing: analysis and comparisons to static load experiments", *Trib. Transactions*, **54** (3), pp. 370-383.
- (16) C.C. Lee, H.I. You (2010), "Geometrical design considerations on externally pressurized porous gas bearings", *Trib. Transactions*, **53** (3), pp. 386-391.
- (17) M. Carpino, G. Talmage (2010), "Minimum Film Thickness in a Gas Foil Journal Bearing with an Unbalanced Rotor", *Trib. Transactions*, **53** (3), pp.433-439.

- (18)B. Terp Paulsen , S. Morosi , I. F. Santos (2011), “Static, Dynamic, and Thermal Properties of Compressible Fluid Film Journal Bearings”, Trib. Transactions, **54** (2), pp. 282-299.
- (19)Fan K.-C., Ho C.-C., Mou J.-I. (2002) “Development of a multiple-microhole aerostatic air bearing system”, Journal of Micromechanics and Microengineering, **12**, pp. 636-643.
- (20)Miyatake M., Yoshimoto S. (2010) “Numerical investigation of static and dynamic characteristics of aerostatic thrust bearings with small feed holes”, Tribol. Intern. **43**, pp.1353-1359.
- (21)Belforte G., Colombo F., Raparelli T., Trivella A., Viktorov V. (2010), “A new identification method of the supply hole discharge coefficient of gas bearings”, 3<sup>th</sup> International Conference on Tribology and Design, WIT Transaction on Engineering Sciences, **66**, pp. 5-105.